

# Topological order and criticality in (2+1)D monitored random quantum circuits

Ali Lavasani<sup>1,2</sup>, Yahya Alavirad<sup>1,2,3</sup>, Maissam Barkeshli<sup>1,2</sup>

<sup>1</sup>*Condensed Matter Theory Center, University of Maryland, College Park, Maryland 20742, USA*

<sup>2</sup>*Joint Quantum Institute, University of Maryland, College Park, Maryland 20742, USA and*

<sup>3</sup>*Department of Physics, University of California at San Diego, La Jolla, CA 92093, USA*

It has recently been discovered that random quantum circuits provide an avenue to realize rich entanglement phase diagrams, which are hidden to standard expectation values of operators. Here we study (2+1)D random circuits with random Clifford unitary gates and measurements designed to stabilize trivial area law and topologically ordered phases. With competing single qubit Pauli-Z and toric code stabilizer measurements, in addition to random Clifford unitaries, we find a phase diagram involving a tricritical point that maps to (2+1)D percolation, a possibly stable critical phase, topologically ordered, trivial, and volume law phases, and lines of critical points separating them. With Pauli-Y single qubit measurements instead, we find an anisotropic self-dual tricritical point, with dynamical exponent  $z \approx 1.46$ , exhibiting logarithmic violation of the area law and an anomalous exponent for the topological entanglement entropy, which thus appears distinct from any known percolation fixed point. The phase diagram also hosts a measurement-induced volume law entangled phase in the absence of unitary dynamics. We also propose a definition of phases of quantum random circuits which is motivated by our numerical results.

*Introduction* - In the past few years, it has been realized that the interplay between measurements and unitary dynamics can give rise to rich physics in the dynamics of quantum entanglement [1–37]. Originally, it was shown that when (1+1)D random unitary dynamics are intercepted by local measurements at a rate  $p$ , the system can undergo a phase transition from a volume law entangled phase at  $p < p_c$  to an area law entangled phase at  $p > p_c$  [1–3]. Importantly, these phase transitions are entirely hidden from simple expectation values of operators but are manifest in *quantum-trajectory averaged* dynamics of entanglement measures, like the entanglement entropy (EE) [1, 2, 4, 21].

Recently, it was shown that competing measurement protocols can give rise to entanglement transitions even in the absence of unitary dynamics [21, 22, 28, 34]. Furthermore, it was discovered that distinct (1+1)D area law phases, i.e. symmetry-protected topological (SPT) [21] and symmetry-broken [22] phases can remain well-defined in the context of random quantum circuits [38].

In this work, we consider a class of (2+1)D random quantum circuits that extrapolate between (1) a topologically ordered phase, characterized by non-zero topological entanglement entropy (TEE) [39, 40] and realized by measuring the  $\mathbb{Z}_2$  toric code stabilizers [41], (2) a volume law entangled phase realized by random Clifford unitaries, and, (3) the trivial, area law phase realized by single-site projective measurements. This generalizes the work of Ref. [21] to (2+1)D where symmetry restrictions are not necessary. Similar to Ref. [21], at each step of the circuit, an element corresponding to one of the three phases is selected at random with probability  $p_g$ ,  $p_u$ ,  $p_s$  respectively (subject to the condition  $p_g + p_s + p_u = 1$ ).

Two typical arrangements of our circuits together with numerically calculated phase diagrams are shown

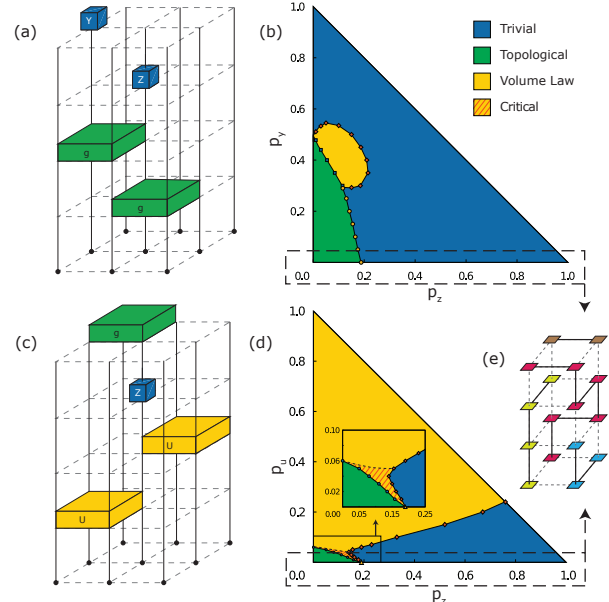


FIG. 1. (a) A typical projective random circuit comprised of toric code stabilizer, single qubit Z and single qubit Y measurements. (b) Phase diagram of (2+1)D projective random circuits. (c) A typical hybrid random circuit comprised of random Clifford unitaries in addition to toric code stabilizer and single qubit Z measurements. (d) Phase diagram of (2+1)D hybrid random circuits. (e) The entanglement dynamics at the  $p_y = 0$  line of (2+1)D projective random circuits (as well as the  $p_u = 0$  line of (2+1)D hybrid random circuits) maps to a 3D bond percolation problem on a cubic lattice.

in Fig. 1. We find stable topological, trivial area law, volume law (even in the absence of unitary dynamics), and critical phases in the phase diagram. Notably, we also find evidence of several qualitatively distinct multi-critical points.

In the absence of unitary dynamics and in the case where single qubits are only measured in the Pauli- $Z$  (or  $X$ ) basis, we find an exact analytical mapping between a 3D classical bond percolation problem and the dynamics of entanglement in the quantum circuit. We show that EE of rectangular regions in the quantum circuit are related to the number of clusters shared between that region and the rest of the system in the classical percolation problem.

In the absence of unitary dynamics and in the case where single qubits are only measured in the  $Y$  direction,

we show that an Ising duality restricts the phase diagram. At the self-dual point  $(p_z, p_y) = (0, 0.5)$ , we find a novel tricritical point separating topological, trivial area law, and volume law phases, in which the critical behavior of the system is qualitatively different from the rest of the phase diagram. Intriguingly, the circuit has non-trivial subsystem symmetries at this point.

We extensively study the phase transitions throughout the phase diagram numerically and find that *away* from the self-dual point discussed above: (1) The critical points are area law entangled, similar to usual  $(2+1)$ D scale invariant field theories. The sub-leading correction to this area-law scaling also agrees with results found in a variety of  $(2+1)$ D scale invariant field theories [42–45] (in contrast to the results of Ref. [30]). (2) We find a correlation length exponent  $\nu = 0.8(1)$  and a dynamical critical exponent  $z = 1$ , which are set by the classical 3D bond percolation theory. Within margin of error, these exponents stay constant along phase boundaries.

However, the critical dynamics at the self-dual  $p_z = 0$ ,  $p_y = 0.5$  point is entirely distinct and characterized by: (1) Logarithmic corrections to the area law scaling of EE reminiscent of Fermi liquids. (2) Non-percolation correlation length exponent  $\nu = 0.47(8)$  and a dynamical critical exponent  $z = 1.46(6)$ . (3) A non-zero anomalous  $\gamma = 1.0(2)$  exponent for the TEE (see Eq. (3)).

*Models* - We consider a system of  $N = L^2$  qubits laid on a two dimensional square lattice of linear length  $L_x = L_y = L$  with periodic boundary conditions. The qubits are placed on the vertices of the lattice.

We consider three different sets of gates where each gate set, when applied exclusively, drives the system into one of the distinct phases discussed above (topological, trivial area law, and, volume law).

For the topological phase, we consider the set of measurements corresponding to the four qubit  $X$  and  $Z$  stabilizers of the toric code model,

$$g_{i,j} = \begin{cases} X_{i,j} X_{i+1,j} X_{i,j+1} X_{i+1,j+1} & i+j \text{ is even} \\ Z_{i,j} Z_{i+1,j} Z_{i,j+1} Z_{i+1,j+1} & i+j \text{ is odd} \end{cases}, \quad (1)$$

where  $(i, j)$  denotes the coordinates on the lattice and  $X_{i,j}$  and  $Z_{i,j}$  are the Pauli operators acting on the corresponding qubit.

We denote the set of all  $g_{i,j}$  operators as  $\mathcal{M}_g$ .

For the trivial phase, we can pick any set of single qubit measurements. We use  $\mathcal{M}_P$  to denote the set of single qubit Pauli- $P$  operators.

Finally, for the volume law phase, we use the set  $\mathcal{C}_4$  consisting of four qubit Clifford unitaries  $U_{i,j}$ , acting on neighboring qubits located at  $(i, j)$ ,  $(i+1, j)$ ,  $(i, j+1)$  and  $(i+1, j+1)$ .

*Projective Random Quantum Circuits* - We study two types of random circuits in this work. First, we consider projective random circuits, which are comprised of only measurements. More specifically, we start with the product state  $|0\rangle^{\otimes N}$  and at each updating step, we measure an operator which is chosen uniformly at random from either  $\mathcal{M}_Z$  with probability  $p_z$ ,  $\mathcal{M}_Y$  with probability  $p_y$  or  $\mathcal{M}_g$  with probability  $p_g = 1 - p_z - p_y$ . Each time step is defined as  $N$  consecutive updating steps. A typical example of such a circuit is shown in Fig. 1a.

*Hybrid Random Quantum Circuits* - We also consider hybrid quantum circuits, which are comprised of unitary gates randomly chosen from  $\mathcal{C}_4$  and measurements of operators taken randomly from  $\mathcal{M}_g$  and  $\mathcal{M}_Z$ . We start with the product state  $|0\rangle^{\otimes N}$  as before, but now at each updating step we either apply a gate chosen uniformly at random from  $\mathcal{C}_4$  with probability  $p_u$  or measure an operator chosen uniformly at random from  $\mathcal{M}_Z$  or  $\mathcal{M}_g$  with probabilities  $p_z$  and  $p_g = 1 - p_u - p_z$  respectively.

*Order Parameters* - One can use TEE [39, 40] to distinguish phases. To find the TEE, we consider a square region of side  $L/2$  and cut it into three disjoint regions:  $A$  (a  $L/2 \times L/4$  rectangle),  $B$  and  $C$  (squares of side  $L/4$ ). The TEE is then given as,

$$S_{\text{topo}} = S_{AB} + S_{BC} + S_{AC} - S_A - S_B - S_C - S_{ABC} \quad (2)$$

$S_{\text{topo}}$  equals 1 for the eigenstates of the toric code Hamiltonian while it is 0 for quantum states in the trivial phase. As for the volume law phase, the contribution which is proportional to the size of each region cancels out and one may expect  $S_{\text{topo}}$  to vanish in this phase as well. However, the  $(1+1)$ D results [4, 35] suggest that the EE of a region has sub-extensive contributions (power-law or logarithmic [33, 35] in its size). As a result, we expect these sub-extensive contributions to the EE to survive and hence result in a system-size dependent value for  $S_{\text{topo}}$ , which in turn can be used to identify the volume law phase. Our numerical results support this scenario.

In addition to TEE, we also utilize the ancilla order parameter introduced in Refs. [5, 6] which captures the transition in purification dynamics. It is defined using  $N_a$  ancilla qubits in addition to the system qubits, as follows. First a constant depth random non-local Clifford unitary is applied on the entire set of qubits, which results in a maximally entangled stabilizer state of all qubits. Next, the system qubits are evolved under the random quantum circuit of interest for  $T$  time-steps and then the EE of the set of all ancilla qubits, denoted by  $S_a(T)$ , is measured. In the  $T \rightarrow \infty$  limit, the ancilla system will be

entirely disentangled from the system. However, this purification dynamics happens with a rate which depends on the phase of the system. In the trivial area law phase, the ancilla qubits will be disentangled in constant time, independent of the system size. In the topological phase, although the bulk disentangles in constant time, the logical qubits remain entangled with the ancilla system until a time exponentially large in system size. In the volume law phase, the bulk remains entangled with the ancilla qubits up to exponentially large time-steps. Therefore for large enough system sizes and at  $T = \mathcal{O}(L)$ ,  $S_a(T)$  will be 0,  $N_L$  and  $N_a$  in trivial, topological and volume law phases respectively, where  $N_L$  denotes the number of logical qubits in the topological phase ( $N_L = 2$  for the torus topology). Note we assume that  $N_L \ll N_a \ll L^2$ . We use  $N_a = 10$  ancillas throughout this work.

We note that while in our setting the purification transition occurs concurrently with TEE phase transition, they are not exactly the same[5]. One can, for instance, repeat the study here on a triangulation of a 2-sphere, for which  $N_L = 0$ , so purification protocols cannot distinguish the trivial and topological phases, while the TEE can. We also note that the proposal of Ref.[6] to detect the purification phase transition in experiments cannot be carried out efficiently in our circuits, because the ancilla system needs to be entangled with the logical qubits, which are non-local in the physical qubits. As such, it remains unclear to what extent it is possible to efficiently distinguish the topological and trivial phases experimentally.

*Results* - We are now in a position to present the numerical results. All values are obtained via averaging over  $\mathcal{O}(10^3) - \mathcal{O}(10^4)$  quantum trajectories, after running the circuit for  $\mathcal{O}(L)$  time-steps to reach the steady state.

*Projective random circuit* - We start by studying the phase diagram of the projective random circuits, which contains no unitary dynamics, i.e.  $p_u = 0$ . First, we focus on the  $p_y = 0$  line of the phase diagram. Notably, as shown in the Supplemental Material, there is an exact mapping which maps the entanglement dynamics at this line of the phase diagram to a classical bond percolation problem on a 3D cubic lattice. Fig. 2a and b show the TEE and the ancilla order parameter as a function of  $p_z$ . As can be seen from the plots, there exists a stable topological phase extending up to  $p_c \approx 0.2$ , at which point a continuous phase transition takes the system to the trivial phase.

On general grounds, we may assume the following scaling forms governing the order parameters near the phase transition[46]

$$S_{\text{topo}}(p; L) = L^\gamma F((p - p_c)L^{1/\nu}), \quad (3)$$

$$S_a(p, t, L) = G((p - p_c)L^{1/\nu}, t/L^z), \quad (4)$$

where  $F(x)$  and  $G(x)$  are arbitrary functions and  $\nu$  and  $z$  are the correlation length critical exponent and dynam-

ical critical exponent respectively. We find our data for the percolation critical point to be consistent with setting  $\gamma$  to 0. By collapsing  $S_{\text{topo}}$  near the critical point for different system sizes, we find  $p_c = 0.188(2)$  and  $\nu = 0.85(6)$ . Note that  $\nu$  is consistent with the values obtained from numerical simulation of classical percolation in 3D[47]. By investigating the time dependence of the ancilla order parameter  $S_a$  at  $p = p_c$ , we find it to be consistent with  $z = 1$  (see Supplemental Material for relevant plots). Collapsing  $S_a$  at  $t = O(L)$  then yields  $\nu = 0.88(7)$ , in agreement with the value found via collapsing  $S_{\text{topo}}$ .

Another quantity of interest is the scaling form of the EE with sub-system size at the critical point. We consider the cylindrical region  $R$  with a smooth boundary, which has length  $x$  in one direction and goes all the way around the torus in the other direction. Let  $S_R(x)$  denote its EE. Note that the boundary length  $|\partial R|$  is  $2L$ , independent of  $x$ . As is discussed in the Supplemental Material, in the percolation picture this quantity is related to the number of clusters with shared support on region  $R$  and its complement.

For a conventional CFT in  $(2+1)$ D, the leading area-law term scales with  $|\partial R|$ , with a coefficient which is not universal in general. The sub-leading term for a cylindrical subregion is less well-understood and several forms have been suggested, among which two are of particular interest. One is a quasi- $(1+1)$ D scaling function, inspired by the exact form found in  $(1+1)$ D CFTs, which seems to decently capture the EE scaling in certain  $(2+1)$ D gapless models [43]:

$$S_R^{\text{q1D}}(x) = b + a \log\left(\frac{L}{\pi} \sin\left(\frac{\pi x}{L}\right)\right), \quad (5)$$

where  $b$  contains the non-universal area law term. The other relevant scaling form was originally derived for the quantum Lifshitz model[44] but was found to describe the EE scaling in various other  $(2+1)$ D gapless models as well, including some  $(2+1)$ D CFTs [42].

$$S_R^{\text{qlm}}(x) = b + a J_\lambda(x/L) \quad (6)$$

$$J_\lambda(u) = \log\left(\frac{\theta_3(i\lambda u)\theta_3(i\lambda(1-u))}{\eta(2iu)\eta(2i(1-u))}\right), \quad (7)$$

where  $\theta_3(z)$  and  $\eta(z)$  are the Jacobi theta function and the Dedekind eta function respectively (see Supplemental Material for definitions).  $b$  contains the non-universal area-law contribution and  $\lambda$  is a model parameter, which we will use to find the best fit.

Fig. 2c shows  $S_R(x)$  for system size  $L = 64$  at  $p_c$  alongside the best fit of the scaling functions. As can be seen from the graph,  $S_R^{\text{qlm}}(x)$  results in a good fit (solid line), while  $S_R^{\text{q1D}}$  cannot capture the scaling form. Moreover, we find that the best fit values of  $a = -1.16(1)$  and  $\lambda = 0.91(5)$  for  $S_R^{\text{qlm}}$  remain constant for different

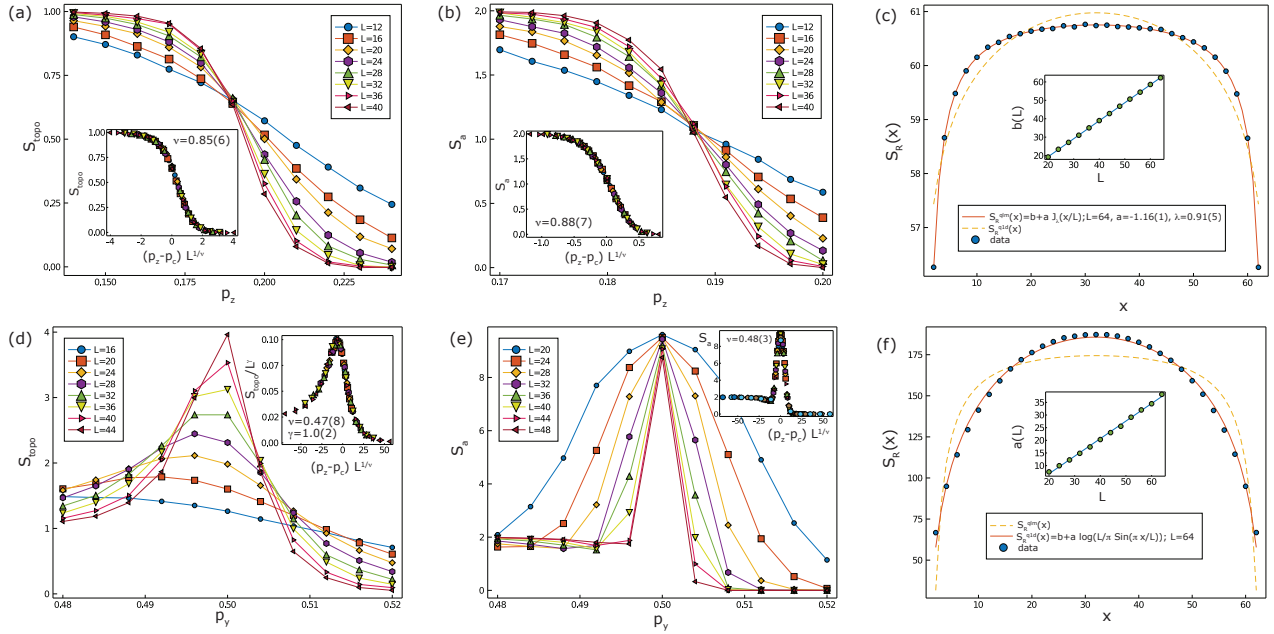


FIG. 2. (a)  $S_{\text{topo}}$  and (b)  $S_a$  measured at  $t = 4L$  as a function of  $p_z$  for fixed  $p_y = 0$ . The insets show the data collapse according to scaling forms in Eq.(3) with  $z = 1$  and  $\gamma = 0$ . (c)  $S_R$  as a function of its length  $x$ , for system size  $L = 64$  at the percolation critical point, with the best fit of scaling functions  $S^{\text{qlm}}(x)$  (solid line) and  $S^{\text{q1D}}$  (dashed line). The inset is the best fit value of the  $b$  parameter in Eq.(6) as a function of  $L$ , which shows a clear area law leading term. (d)  $S_{\text{topo}}$  and (e)  $S_a$  measured at  $t = 0.6L^{1.46}$  as a function of  $p_y$  for fixed  $p_z = 0$ . The insets show data collapse. (f)  $S_R$  as a function of its length  $x$  for system size  $L = 64$  at the self-dual critical point  $(p_z, p_y) = (0, 0.5)$ , with the best fit of scaling functions  $S^{\text{q1D}}$  (solid line) and  $S^{\text{qlm}}(x)$  (dashed line). The inset shows the linear dependence of the best fit value of the  $a$  parameter in Eq.(5), which is an evidence of  $L \log L$  scaling of the EE.

system sizes within the margin of error (see Supplemental Material). As is shown in the inset, the  $b$  parameter scales linearly with system size, which shows that the leading term scales with  $|\partial R|$ .

We now turn our attention to the  $p_z = 0$  line. Here the circuit has a self-duality mapping  $p_y \rightarrow 1 - p_y$ . Note that along this line, the system has  $2L$  subsystem symmetries generated by the product of  $Y$  (or stabilizer) operators along horizontal or vertical loops, e.g.  $\prod_j Y_{i,j}$ . On a related note, there is a unitary transformation which maps the  $g$  and  $Y$  operators to the gauge operators of the 2D Bacon-Shor subsystem code[48, 49] on a square lattice (see the Supplemental Material for details).

By examining the TEE  $S_{\text{topo}}$ (Fig. 2d), we find the topological phase to be extended up to the self-dual point  $p_y = 0.5$ . However, at  $p_y = 0.5$ ,  $S_{\text{topo}}$  grows with system size, which suggests a non-zero  $\gamma$  exponent. Collapsing  $S_{\text{topo}}$  data near the critical point yields  $p_c = 0.502(1)$ ,  $\gamma = 1.0(2)$  and  $\nu = 0.47(8)$ , which shows that this critical point is distinct from the percolation fixed point [50]. Moreover, by looking at the time dependence of the ancilla order parameter at  $p_y = 0.5$ , we find that, in contrast to the percolation critical point, the best fit to the scaling form in Eq. 3 corresponds to  $z = 1.46(8)$  (see Supplemental Material for relevant plots). Accordingly, by collapsing  $S_a(p, t, L)$  data at  $t = O(L^{1.46})$  (Fig. 2e),

we find  $\nu = 0.48(3)$ , in agreement with the result obtain from collapsing  $S_{\text{topo}}$ .

As for the cylindrical subregion EE  $S_R(x)$  (Fig. 2f), we find that the quasi-1d scaling form  $S^{\text{q1D}}(x)$  – rather than  $S^{\text{qlm}}(x)$  – fits the data. However, as is shown in the inset, the  $a$  parameter in Eq.(6) is not constant, but has a linear dependence on system size  $L$ , demonstrating that the leading term scales as  $L \log L$  rather than  $L$  as is expected in an area law state. The origin of the  $L \log L$  violation is unclear; it may be related to the existence of subsystem symmetries along the  $p_z = 0$  axis. A logarithmic violation of the area law in (2+1)D random quantum circuits has also been reported in Refs. [28, 30], although the precise connection to the fixed point studied here is unclear.

The rest of the phase diagram can be determined analogously (Fig. 1a). We find that the percolation critical point is part of a critical line that persists up to some finite non-zero value of  $p_y$ , while the self-dual critical point at  $(p_z, p_y) = (0, 0.5)$  splits into two critical lines with an intermediate volume law entangled phase in between, making it tricritical. Interestingly, the numerical data for all critical points that we considered, other than  $(p_z, p_y) = (0, 0.5)$ , are consistent with  $z = 1$  and  $\gamma = 0$ , with  $\nu$  remaining close to 0.8, similar to the percolation critical point. Their EE scaling is given by  $S^{\text{qlm}}(x)$  as

well, with an area law scaling leading term. Remarkably, this makes the self-dual point special in this regard, as it is the only point in the phase diagram with  $L \log L$  violation of area law, as well as quite different  $\nu$  and  $\gamma$  exponents. We also note that the extracted  $a$  and  $\lambda$  parameters in  $S^{\text{qlm}}(x)$  change throughout the phase diagram. The relevant plots can be found in the Supplemental Material.

*Hybrid random circuit-* We now consider the hybrid random circuit, comprised of random 4-qubit unitary gates, toric code stabilizer measurements and single qubit  $Z$  measurements. The  $p_u = 0$  line of the phase diagram is exactly the same as the  $p_z = 0$  line of the projective random circuit phase diagram, with the same percolation phase transition occurring at  $p_z = 0.188(2)$ . Fig. 3a shows the ancilla order parameter along the  $p_u = 0.01$  line, which shows the emergence of an intervening phase between the topological and trivial phases, which suggests that the percolation critical point is actually a tricritical point in this phase diagram. In the intermediate phase,  $S_a$  does not saturate to  $N_a = 10$ , as is expected to be the case in the volume law phase, but rather increases weakly with system size, showing indications that it may saturate at a finite value less than 10. Indeed, for a point in the intermediate phase and for large systems,  $S_a(t; L)$  seems to be a function of only  $t/L$  (Fig. 3b) which is a signature of a critical phase with  $z = 1$  (see Eq. 4). Moreover, we find that in the intermediate phase,  $S^{\text{qlm}}(x)$  fits the EE of a cylindrical subregion as well. These points suggest that the intermediate phase is a critical region.

The critical region extends to the  $p_u$  axis, ending at  $p_u \approx 0.06$ , which appears to be a tricritical point, although within the precision of this study, we cannot rule out the existence of a narrow critical region around  $p_u = 0.06$ . By collapsing the  $S_a$  data along the  $p_u$  axis, we find  $p_c = 0.059(1)$  with critical exponent  $\nu = 0.78(8)$ . On the right, the critical region ends on the boundary of the trivial phase and the volume law phase. The trivial phase itself ends at  $p_u = 0.238(2)$  along the  $p_u + p_z = 1$  line. We find  $\nu = 0.80(7)$  at the corresponding phase transition (see the Supplemental Material for relevant plots). The overall phase diagram of the hybrid circuit in 2D is illustrated in Fig. 1b.

*Outlook* - The finding of this study as well as previous studies [21, 22, 28] suggests the emergence of robust phases of matter in the context of random quantum circuits. Nonetheless, a formal definition of the notion of a phase of a random quantum circuit is still lacking. The standard definitions of phases of matter are not applicable here because (1) the system is not described by a fixed Hamiltonian but only via a probability distribution over a set of quantum gates (including measurements) and (2) the steady state density matrix of the system is featureless and the rich entanglement structure is only visible at the level of individual quantum trajectories which never reach a fixed state. Notably, due to the presence of mea-

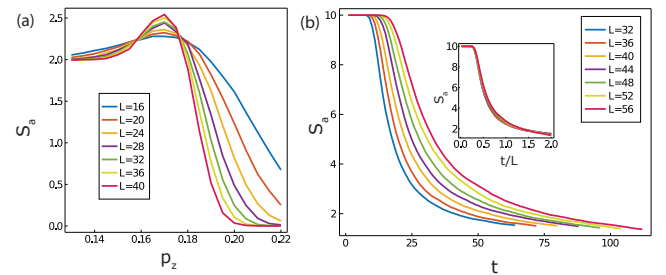


FIG. 3. (a) The ancilla EE  $S_a$  measured at  $t = L$  as a function of  $p_z$  for fixed  $p_u = 0.01$  in the hybrid random circuit. (b)  $S_a$  as a function of time at  $(p_z, p_u) = (0.17, 0.01)$ . The inset is the same, plotted as a function of  $t/L$ .

surements, the existence of a finite Lieb-Robinson bound in these systems is still unclear[34, 51]. To account for these points and based on our results, we propose the following formal classification of random quantum circuits into distinct topological classes:

**Definition 1.** *Given two quantum states  $|\psi\rangle$  and  $|\phi\rangle$ , let  $d_{\psi, \phi}$ , called the circuit distance, denote the minimum depth of a local unitary circuit which transforms one into another. Given two probability distributions  $P_1$  and  $P_2$  over the quantum states in a Hilbert space  $\mathcal{H}$ , let  $d_{P_1, P_2}$  denote the average circuit distance between two states which are picked according to the corresponding probability distribution, i.e.*

$$d_{P_1, P_2} \equiv \sum_{|\psi\rangle, |\phi\rangle \in \mathcal{H}} P_1(|\psi\rangle) P_2(|\phi\rangle) d_{\psi, \phi}. \quad (8)$$

Let  $\mathcal{Q}_N = \{Q_{N,t}\}_{t=1}^{\infty}$ , with  $Q_{N,t}$  a probability distribution over depth- $t$  quantum circuits (composed of unitaries and measurements) acting on  $N$  qubits. Let  $P_{\mathcal{Q};N}(t)$  denote the probability distribution describing the output quantum state of a random circuit chosen according to probability distribution  $Q_{N,t}$  and applied to  $|0\rangle^{\otimes N}$  state. We define  $P_{\mathcal{Q};N} \equiv \lim_{t \rightarrow \infty} P_{\mathcal{Q};N}(t)$ , assuming such a limit exists.

Finally, we say two families of quantum random circuits  $\{\mathcal{Q}_N\}_{N=1}^{\infty}$  and  $\{\mathcal{Q}'_N\}_{N=1}^{\infty}$  describe the same topological phase if and only if

$$\lim_{N \rightarrow \infty} d_{P_{\mathcal{Q};N}, P_{\mathcal{Q}';N}} < c, \quad (9)$$

for some finite  $c$ .

Note that area law entangled states can not become volume law entangled under a constant depth local unitary circuit because such circuits can not generate long range entanglement. Moreover, a state with non-zero TEE can not be transformed into a product state in constant depth using local unitaries[52]. Hence, we expect that the proposed classification results in the same partitioning of the phase diagram as we observed here numerically. We leave a detailed study of the implications of this definition to future studies.

*Acknowledgements* - We thank Michael Gullans for discussions. The authors acknowledge the University of Maryland supercomputing resources (<http://hpcc.umd.edu>) made available for conducting the research reported in this paper. A.L and M.B are supported by NSF CAREER (DMR- 1753240), Alfred P. Sloan Research Fellowship, and JQI- PFC-UMD. Y.A is supported by Simons Collaboration on Ultra-Quantum Matter, grant 651440 from the Simons Foundation as well as University of California Laboratory Fees Research Program, grant LFR-20-653926.

---

[1] B. Skinner, J. Ruhman, and A. Nahum, *Physical Review X* **9**, 031009 (2019).

[2] Y. Li, X. Chen, and M. P. Fisher, *Physical Review B* **98**, 205136 (2018).

[3] A. Chan, R. M. Nandkishore, M. Pretko, and G. Smith, *Phys. Rev. B* **99**, 224307 (2019).

[4] Y. Li, X. Chen, and M. P. Fisher, *Physical Review B* **100**, 134306 (2019).

[5] M. J. Gullans and D. A. Huse, arXiv preprint arXiv:1905.05195 (2019).

[6] M. J. Gullans and D. A. Huse, *Phys. Rev. Lett.* **125**, 070606 (2020).

[7] R. Vasseur, A. C. Potter, Y.-Z. You, and A. W. W. Ludwig, *Phys. Rev. B* **100**, 134203 (2019).

[8] S. Choi, Y. Bao, X.-L. Qi, and E. Altman, “Quantum error correction in scrambling dynamics and measurement induced phase transition,” (2019), arXiv:1903.05124.

[9] M. Szyniszewski, A. Romito, and H. Schomerus, *Phys. Rev. B* **100**, 064204 (2019).

[10] Q. Tang and W. Zhu, *Phys. Rev. Research* **2**, 013022 (2020).

[11] C.-M. Jian, Y.-Z. You, R. Vasseur, and A. W. W. Ludwig, *Phys. Rev. B* **101**, 104302 (2020).

[12] X. Cao, A. Tilloy, and A. D. Luca, *SciPost Phys.* **7**, 24 (2019).

[13] J. Lopez-Piqueres, B. Ware, and R. Vasseur, “Mean-field theory of entanglement transitions from random tree tensor networks,” (2020), arXiv:2003.01138.

[14] Y. Bao, S. Choi, and E. Altman, *Phys. Rev. B* **101**, 104301 (2020).

[15] L. Piroli, C. Sünderhauf, and X.-L. Qi, “A random unitary circuit model for black hole evaporation,” (2020), arXiv:2002.09236.

[16] A. Zabalo, M. J. Gullans, J. H. Wilson, S. Gopalakrishnan, D. A. Huse, and J. H. Pixley, *Phys. Rev. B* **101**, 060301 (2020).

[17] D. Rossini and E. Vicari, “Measurement-induced dynamics of many-body systems at quantum criticality,” (2020), arXiv:2001.11501.

[18] J. Iaconis, A. Lucas, and X. Chen, “Measurement-induced phase transitions in quantum automaton circuits,” (2020), arXiv:2010.02196 [quant-ph].

[19] Y. Fuji and Y. Ashida, *Phys. Rev. B* **102**, 054302 (2020).

[20] N. Lang and H. P. Büchler, *Phys. Rev. B* **102**, 094204 (2020).

[21] A. Lavasani, Y. Alavirad, and M. Barkeshli, “Measurement-induced topological entanglement transitions in symmetric random quantum circuits,” (2020), arXiv:2004.07243 [quant-ph].

[22] S. Sang and T. H. Hsieh, “Measurement protected quantum phases,” (2020), arXiv:2004.09509 [cond-mat.stat-mech].

[23] X. Chen, Y. Li, M. P. A. Fisher, and A. Lucas, *Phys. Rev. Research* **2**, 033017 (2020).

[24] A. Nahum, S. Roy, B. Skinner, and J. Ruhman, “Measurement and entanglement phase transitions in all-to-all quantum circuits, on quantum trees, and in landau-ginsburg theory,” (2020), arXiv:2009.11311 [cond-mat.stat-mech].

[25] O. Lunt and A. Pal, *Phys. Rev. Research* **2**, 043072 (2020).

[26] M. Szyniszewski, A. Romito, and H. Schomerus, “Universality of entanglement transitions from stroboscopic to continuous measurements,” (2020), arXiv:2005.01863 [cond-mat.stat-mech].

[27] M. J. Gullans, S. Krastanov, D. A. Huse, L. Jiang, and S. T. Flammia, “Quantum coding with low-depth random circuits,” (2020), arXiv:2010.09775 [quant-ph].

[28] A. Nahum and B. Skinner, *Phys. Rev. Research* **2**, 023288 (2020).

[29] O. Alberton, M. Buchhold, and S. Diehl, “Trajectory dependent entanglement transition in a free fermion chain – from extended criticality to area law,” (2020), arXiv:2005.09722 [cond-mat.stat-mech].

[30] X. Turkeshi, R. Fazio, and M. Dalmonte, *Phys. Rev. B* **102**, 014315 (2020).

[31] L. Fidkowski, J. Haah, and M. B. Hastings, “How dynamical quantum memories forget,” (2020), arXiv:2008.10611 [quant-ph].

[32] S. Vijay, “Measurement-driven phase transition within a volume-law entangled phase,” (2020), arXiv:2005.03052 [quant-ph].

[33] R. Fan, S. Vijay, A. Vishwanath, and Y.-Z. You, “Self-organized error correction in random unitary circuits with measurement,” (2020), arXiv:2002.12385 [cond-mat.stat-mech].

[34] M. Ippoliti, M. J. Gullans, S. Gopalakrishnan, D. A. Huse, and V. Khemani, “Entanglement phase transitions in measurement-only dynamics,” (2020), arXiv:2004.09560 [quant-ph].

[35] Y. Li and M. P. A. Fisher, “Statistical mechanics of quantum error-correcting codes,” (2020), arXiv:2007.03822 [quant-ph].

[36] M. Van Regemortel, Z.-P. Cian, A. Seif, H. Dehghani, and M. Hafezi, arXiv preprint arXiv:2008.08619 (2020).

[37] O. Shtanko, Y. A. Kharkov, L. P. Garcí-Pintos, and A. V. Gorshkov, “Classical models of entanglement in monitored random circuits,” (2020), arXiv:2004.06736 [cond-mat.dis-nn].

[38] Distinct volume law phases have also been recently discussed in Refs. [24, 32].

[39] A. Kitaev and J. Preskill, *Phys. Rev. Lett.* **96**, 110404 (2006).

[40] M. Levin and X.-G. Wen, *Phys. Rev. Lett.* **96**, 110405 (2006).

[41] A. Kitaev, *Annals of Physics* **303**, 2 (2003).

[42] X. Chen, G. Y. Cho, T. Faulkner, and E. Fradkin, *Journal of Statistical Mechanics: Theory and Experiment* **2015**, P02010 (2015).

[43] H. Ju, A. B. Kallin, P. Fendley, M. B. Hastings, and R. G. Melko, *Phys. Rev. B* **85**, 165121 (2012).

- [44] J.-M. Stephan, H. Ju, P. Fendley, and R. G. Melko, *New Journal of Physics* **15**, 015004 (2013).
- [45] A. B. Kallin, E. Stoudenmire, P. Fendley, R. R. Singh, and R. G. Melko, *Journal of Statistical Mechanics: Theory and Experiment* **2014**, P06009 (2014).
- [46] Note that since  $S_a \leq 10$ , its scaling form can not have a  $L^\gamma$  prefactor.
- [47] J. Wang, Z. Zhou, W. Zhang, T. M. Garoni, and Y. Deng, *Phys. Rev. E* **87**, 052107 (2013).
- [48] D. Bacon, *Phys. Rev. A* **73**, 012340 (2006).
- [49] P. W. Shor, *Phys. Rev. A* **52**, R2493 (1995).
- [50] The  $p_c - 0.5$  difference is probably due to finite size effects, since if there is a single critical point, the duality enforces it to be at  $p_y = 0.5$ .
- [51] Y. Li, X. Chen, A. W. W. Ludwig, and M. P. A. Fisher, “Conformal invariance and quantum non-locality in hybrid quantum circuits,” (2020), arXiv:2003.12721.
- [52] X. Chen, Z.-C. Gu, and X.-G. Wen, *Phys. Rev. B* **82**, 155138 (2010).
- [53] C. Xu and J. E. Moore, *Phys. Rev. Lett.* **93**, 047003 (2004).
- [54] Z. Nussinov and J. van den Brink, *Rev. Mod. Phys.* **87**, 1 (2015).
- [55] J. Dorier, F. Becca, and F. Mila, *Phys. Rev. B* **72**, 024448 (2005).
- [56] H.-D. Chen, C. Fang, J. Hu, and H. Yao, *Phys. Rev. B* **75**, 144401 (2007).
- [57] C. Fieker, W. Hart, T. Hofmann, and F. Johansson, in *Proceedings of the 2017 ACM on International Symposium on Symbolic and Algebraic Computation*, ISSAC '17 (ACM, New York, NY, USA, 2017) pp. 157–164.

## Supplemental Material

### Percolation Mapping

In this section we present the mapping between the random quantum circuit with only stabilizers and single qubit  $Z$  measurements to a classical bond percolation problem on the 3D cubic lattice. The quantum circuit could be viewed as either the  $p_y = 0$  line of the projective random quantum circuit or the  $p_u = 0$  line of the hybrid random quantum circuit.

For simplicity, we consider the infinite plane geometry so we can ignore the non-trivial cycles of the torus as well as the subtleties arising near the boundary. Moreover, we work with the standard version of toric code where the qubits are on the edges and the  $X$  and  $Z$  stabilizers correspond to the star and plaquette operators respectively.

We take the initial state to be the eigenstate of all the star and plaquette operators. Note that since single qubit measurements are only in  $Z$  direction, the system will remain to be an eigenstate of plaquette operators. Therefore, we ignore all plaquette operator measurements in what follows.

We place a square on each vertex which represents the corresponding star operator (Fig.4a). We start with all squares having a unique color. At each time step, the colors are updated as follows

- Whenever a star operator is measured, it acquires its own unique color (Fig.4b)
- Whenever a single qubit is measured, the two adjacent squares acquire the same color (Fig.4c)

As we will show, these rules represent how the stabilizer state of the system evolves. On the other hand, these set of rules arise naturally in a percolation picture. Consider a 3D cubic lattice, henceforth called the percolation lattice, and place a square on each vertex. The vertical direction corresponds to time. If a star operator is *not* measured at time  $t$ , we connect the corresponding squares on the  $(t-1)$ 'th and  $t$ 'th layers. And if a qubit is measured at time  $t$ , we connect the corresponding adjacent squares on the  $t$ 'th layer. At the end, we assign a unique color to each cluster of connected squares. The coloring that will arise is exactly what one would have found if the rules listed above were followed (see Fig.4).

The following proposition shows how the stabilizers specifying the state can be inferred from a given coloring configuration.

**Proposition 1.** *Let  $A^j = \{s_i\}_{i=1}^n$  denote the set of squares corresponding to  $j$ 'th color, in some arbitrary order. Up to a minus sign, the following operators stabilize the state:*

$$\bar{\mathcal{X}}_j = \prod_{i=1}^n \mathcal{X}_{s_i} \quad \text{and} \quad Z_{s_i, s_{i+1}}, \quad (10)$$

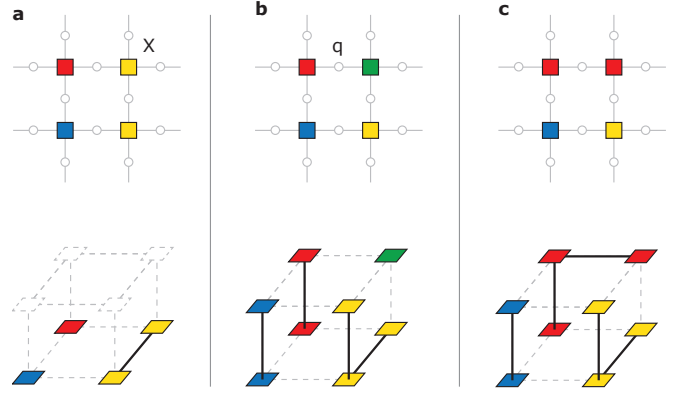


FIG. 4. Diagrammatic representation of coloring rules outlined in the text arise naturally in the 3D percolation picture. (a) The initial coloring of the squares (top) and the corresponding state in the percolation lattice (bottom). (b) The state of the system after the star stabilizer marked by a  $X$  in panel "a" is measured. (c) the state of the system after the qubit marked by  $q$  in panel b is measured in  $Z$  basis.

where  $\mathcal{X}_{s_i}$  is the star operator at square  $s_i$  and  $Z_{s_i, s_{i+1}}$  is the Pauli  $Z$  string operator which starts on  $s_i$  and ends on  $s_{i+1}$ .

Note that, because the quantum state is an eigenstate of every plaquette operator and because the space manifold has trivial topology, we don't need to specify the exact path that  $Z_{s_i, s_{i+1}}$  string operator takes.

*Proof of Proposition 1.* We prove by induction. At  $t = 0$  it is clearly the case.

Now assume it is true at step  $m$ . Let's say we measure the star operator at some vertex  $s_1$  at step  $m+1$ . If the corresponding square has a unique color already, nothing happens and the statement holds trivially afterwards. So let us consider the case where there are more than one squares with the same color as  $s_1$ , denoted by the set  $A^1$ . Based on the induction assumption, the quantum state is an eigenstate of  $\prod_{s \in A^1} \mathcal{X}_s$  operator at step  $m$ . Therefore, after measuring  $\mathcal{X}_{s_1}$ , the system will be an eigenstate of  $\mathcal{X}_{s_1}$  as well as  $\mathcal{X}_{s_1} \times \prod_{s \in A^1 \setminus \{s_1\}} \mathcal{X}_s = \prod_{s \in A^1 \setminus \{s_1\}} \mathcal{X}_s$ . Moreover, any  $Z_{i,j}$  string operator that doesn't end on  $s_1$  commutes with  $\mathcal{X}_{s_1}$  and as such, measurement of  $\mathcal{X}_{s_1}$  has no bearing on the system being an eigenstate of it or not. As for the string operator stabilizers starting or ending on  $s_1$ , one of them will be replaced with  $\mathcal{X}_{s_1}$  stabilizer, and the other with the product of the two which will be an string operator starting and ending on the set  $A^1 \setminus \{s_1\}$ . Ergo the statement holds at step  $m+1$  as well.

Now consider the case in which, at step  $m+1$ , we measure a single qubit – say qubit  $q$  which is between squares  $s_1$  and  $s_2$  – in the  $Z$  basis. If  $s_1$  and  $s_2$  have the same color, it results from the induction hypothesis that

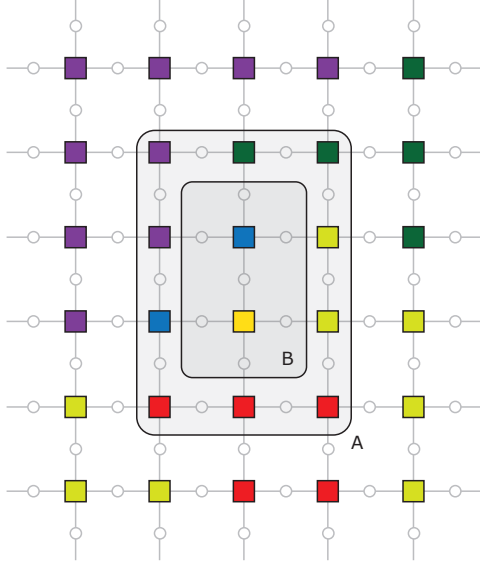


FIG. 5. An example of a rectangular region  $A$  with sides  $l_x = 2$  and  $l_y = 3$ . Its bulk is marked by  $B$ . In the example shown above,  $C_A$  and  $C_B^{\text{ex}}$  have 6 and 1 elements respectively.

$Z_q$  already stabilizes the state and the statement trivially holds at step  $m + 1$ . So let us consider the case where  $s_1$  and  $s_2$  have different colors, such that  $s_1 \in A^1$  and  $s_2 \in A^2$ . Since  $\prod_{s \in A^1 \cup A^2} \mathcal{X}_s$  stabilizes the state at step  $m$  and commutes with  $Z_q$ , it stabilizes the state at step  $m + 1$  as well. Based on the induction assumption, the state is stabilized by any  $Z_{i,j}$  string that has both end points either on  $A^1$  or  $A^2$ . Moreover, it is now stabilized by the string operator which connects  $s_1 \in A^1$  and  $s_2 \in A^2$ , namely  $Z_q$ . Therefore the state of the system at step  $m + 1$  is stabilized by any  $Z_{i,j}$  string that has end points on  $A^1 \cup A^2$ . Hence the statement holds at step  $m + 1$  as well.  $\square$

Proposition 1 allows us to study the entanglement structure of the steady state, using the percolation picture. In particular, the entanglement entropy of a rectangular region  $A$  is equal to the number of clusters which have shared support in  $A$  and  $A^c$ , minus one.

**Proposition 2.** *Let  $A$  be a rectangular region with smooth boundary and let  $B = A \setminus \partial A$  denote its bulk (see Fig. 5). For a given coloring configuration of the squares (star operators), let  $C_A$  denote the set of colors that appear inside  $A$ . Also define  $C_B^{\text{ex}}$  to be the colors that exclusively appear in the bulk. Then, for the stabilizer state which is associated with that coloring, the entanglement entropy of the subset of qubits inside  $A$  can be expressed as,*

$$S_A = |C_A \setminus C_B^{\text{ex}}| - 1. \quad (11)$$

*Proof.* Let  $A$  be a  $l_x \times l_y$  rectangular region. By an abuse of notation, we use  $A$  to denote the set of qubits which

reside inside region  $A$  as well. We prove this claim by direct calculation of the entanglement. For stabilizers states we have

$$S_A = n_A - \dim G_A, \quad (12)$$

where  $n_A$  is the number of qubits in  $A$  and  $G_A$  is the subgroup of stabilizers which act trivially on the qubits in  $A^c$ . It is easy to see that  $G_A$  can be generated by  $Z$  plaquette stabilizers,  $Z_{i,j}$  string stabilizers and  $\bar{X}_j$  stabilizers (see Proposition 1 for their definition) which are themselves contained in  $A$ . Let  $n_{\square}$ ,  $n_S$  and  $n_+$  denote the number of independent  $Z$  plaquette stabilizer,  $Z_{i,j}$  string stabilizer and  $\bar{X}_j$  stabilizers which are contained entirely within  $A$ , respectively. Then we have,

$$S_A = n_A - n_{\square} - n_+ - n_S \quad (13)$$

Now we compute each quantity separately. finding  $n_A$  and  $n_{\square}$  is quite easy,

$$n_A = 2l_x l_y + l_x + l_y, \quad (14)$$

$$n_{\square} = l_x l_y. \quad (15)$$

Also we have  $n_+ = |C_B^{\text{ex}}|$ , because any  $\bar{X}_j$  operator which has a star operator outside  $B$  has nontrivial support in  $A^c$ . For a given color  $c$ , define  $m_{c,A}$  to be the number of squares in  $A$  with color  $c$ . Then we can write  $n_S$  as,

$$n_S = \sum_{c \in C_A} (m_{c,A} - 1) = \sum_{c \in C_A} m_{c,A} - |C_A|. \quad (16)$$

Now, the  $\sum_{c \in C_A} m_{c,A}$  sum is just the total number of squares inside  $A$ , which is  $(l_x + 1)(l_y + 1)$ . Thus we have

$$n_S = l_x l_y + l_x + l_y + 1 - |C_A|. \quad (17)$$

Putting everything together we get,

$$S_A = |C_A| - |C_B^{\text{ex}}| - 1 = |C_A \setminus C_B^{\text{ex}}| - 1, \quad (18)$$

where in the last part we used the fact that  $C_B^{\text{ex}} \subseteq C_A$ .  $\square$

## Duality Mappings

Here, we present the two dualities related to the  $p_z = 0$  line of the projective random circuits, one mapping the circuit at  $p_y$  to the one at  $1 - p_y$  and the other mapping the  $g$  and  $Y$  operators to the gauge operators of the Bacon-Shor code [53, 54]. We start with the first one. Similar to previous section, we consider the infinite plane geometry.

Consider the Clifford unitary  $U$  transforming stabilizer and  $Y$  operators in the following way

$$\begin{aligned} U^\dagger Y_{i,j} U &= g_{i,j} \\ U^\dagger g_{i,j} U &= Y_{i+1,j+1}, \end{aligned} \quad (19)$$

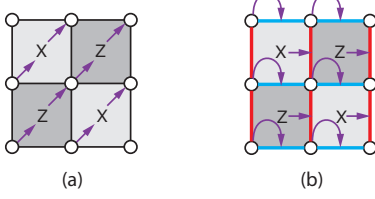


FIG. 6. The diagrammatic illustration of the action of the duality map (a)  $U$  defined by Eqs.(19) and (b)  $\tilde{U}$  defined by Eqs.(20). The white dots correspond to single qubit  $Y$  operators and squares correspond to  $g$  stabilizers. The vertical red lines and horizontal blue lines in panel b represent  $XX$  and  $ZZ$  operators respectively

where  $g_{i,j}$  is defined in Eq.(1), and  $i, j \in \mathbb{Z}$ . Diagrammatically, it acts as a half-translation in both  $i$  and  $j$  directions (see Fig. 6a) such that  $U^2$  is just the lattice translation  $(i, j) \mapsto (i + 1, j + 1)$ .

It is straightforward to verify that this transformation yields the right commutation relations for the images of  $g$  and  $Y$  operators. Clearly, the images of  $Y$  operators commute among themselves, and similarly for the images of the  $g$  operators. On the other hand, note that a stabilizer operator  $g$  anti-commutes only with the four single qubit  $Y$  operators acting on its corners. The  $U$  transformation maps  $g$  to a single qubit  $Y$  operator and maps the four  $Y$  operators to the four neighboring stabilizers, keeping the anti-commutation relations.

To uniquely specify the unitary  $U$ , one has to define its action on a complete basis of Pauli strings. The set of  $Y$  and  $g$  operators is not a complete basis for Pauli strings on an infinite plane and as such, the transformation in (19) does not fully specify  $U$ . However, since the projective random quantum circuits at  $p_z = 0$  are only comprised of  $g$  and  $Y$  measurements, no matter how one extends Eq.(19) to a complete basis, the Clifford  $U$  maps a projective random quantum circuit chosen with probability distribution corresponding to  $p_z = 0$  and  $p_y = p$  to a projective random quantum circuit chosen according to the probability distribution corresponding to  $p_z = 0$  and  $p_y = 1 - p$ .

Moreover, if the stabilizer set describing the state of the system is generated only by operators comprised of  $g$  and  $Y$  operators, Eq.(19) is enough to specify the image of the wave function under  $U$  transformations. It also ensures that  $U$  keeps the local entanglement structure of the state intact, i.e. changing the entanglement of a region by at most a term proportional to the region's area. These considerations then enforce the  $p_z = 0$  line of the phase diagram to be symmetric around  $p_y = 0.5$  point.

The second duality maps the  $Y$  and  $g$  operators to the gauge operators of the Bacon-Shor code. More specifically, consider the Clifford unitary  $\tilde{U}$  which transforms

the stabilizer and  $Y$  operators as

$$\begin{aligned} \tilde{U}^\dagger Y_{i,j} \tilde{U} &= Z_{i,j} Z_{i+1,j} \\ \tilde{U}^\dagger g_{i,j} \tilde{U} &= X_{i+1,j} X_{i+1,j+1}. \end{aligned} \quad (20)$$

It is illustrated diagrammatically in Fig. 6b. As before, we consider the infinite plane geometry. It is easy to verify that  $\tilde{U}$  preserves the commutation relations and hence could be extended to a complete unitary. We note that the measurements of  $g$  and  $Y$  operators, when viewed in the dual picture, resembles the syndrome measurements of the Bacon-Shor subsystem code in the active error correction scheme.

Closely related to the Bacon-Shore code is the quantum compass model on a square lattice defined via the following Hamiltonian,

$$H = -J_Z \sum_{i,j} Z_{i,j} Z_{i+1,j} - J_X \sum_{i,j} X_{i,j} X_{i,j+1}. \quad (21)$$

Interestingly, tuning the coupling ratio  $J_Z/J_X$  drives the system through a first order phase transition at  $J_Z = J_X$  [55, 56].

### Jacobi- $\theta$ functions and Dedekind- $\eta$ function

The Jacobi theta functions are defined for two complex numbers  $z$  and  $\tau$ , where  $\tau$  is assumed to lie in the upper half plane. For a given  $\tau$ , the squared nome  $q$  is defined as

$$q(\tau) = e^{2\pi i \tau}. \quad (22)$$

In terms of  $q$  and  $z$ , the Jacobi- $\theta$  functions are defined as

$$\theta_1(z|\tau) = \sum_{n \in \mathbb{Z}} (-1)^{n-1/2} q^{\frac{1}{2}(n+1/2)^2} e^{i(2n+1)z}, \quad (23)$$

$$\theta_2(z|\tau) = \sum_{n \in \mathbb{Z}} q^{\frac{1}{2}(n+1/2)^2} e^{i(2n+1)z}, \quad (24)$$

$$\theta_3(z|\tau) = \sum_{n \in \mathbb{Z}} q^{\frac{1}{2}n^2} e^{2inz}, \quad (25)$$

$$\theta_4(z|\tau) = \sum_{n \in \mathbb{Z}} (-1)^n q^{\frac{1}{2}n^2} e^{2inz}, \quad (26)$$

$$(27)$$

and the Dedekind- $\eta$  function is given as

$$\eta(\tau) = q^{1/24} \prod_{k=1}^{\infty} (1 - q^k). \quad (28)$$

The one variable  $\theta_\nu(\tau)$  function appearing in Eq.(6) is defined as,

$$\theta_\nu(\tau) = \theta_\nu(0|\tau), \quad \nu = 1, 2, 3, 4. \quad (29)$$

In particular, we have:

$$\theta_3(\tau) = \sum_{n \in \mathbb{Z}} q^{\frac{1}{2}n^2}. \quad (30)$$

To understand the the asymptotic form of the entanglement function  $S^{\text{QLM}}(x)$  for  $x \ll L$ , we need to expand the function  $J(u)$ ,

$$J_\lambda(u) = \log \left( \frac{\theta_3(i\lambda u)\theta_3(i\lambda(1-u))}{\eta(2iu)\eta(2i(1-u))} \right) \quad (31)$$

for small  $u$ . To that end, we use the following identities, related to the modular transformation properties of the Jacobi  $\theta$  functions

$$\theta_3(\tau) = (-i\tau)^{-1/2}\theta_3(-1/\tau) \quad (32)$$

$$\eta(\tau) = (-i\tau)^{-1/2}\eta(-1/\tau). \quad (33)$$

Using the above identities, it is easy to see that for  $\lambda u \ll 1$ ,

$$\theta_3(i\lambda u) \approx (\lambda u)^{-1/2} \quad (34)$$

$$\eta(2iu) \approx (-2u)^{-1/2}e^{-\frac{\pi}{24u}}, \quad (35)$$

which results in the  $1/u$  leading term in the expansion of  $J_\lambda(u)$  at  $\lambda u \ll 1$ ,

$$J_\lambda(u) \approx \frac{\pi}{24}u^{-1} + \text{const.} \quad (36)$$

Note that the coefficient of the leading term is independent of  $\lambda$ .

The Nemo package[57] was used for numerical evaluation of  $\theta_3$  and  $\eta$  functions in this study.

### Estimating Errors

We briefly review the procedure which was utilized in this study to find critical probabilities and critical exponents and explain how their errors were estimated. In general ancilla order parameter yields smoother diagrams and needs less averages, and hence we mostly use  $S_a$  to extract exponents.

Consider a quantity  $S$  which has the following expected scaling form

$$S(p, L) = F((p - p_c)L^{1/\nu}), \quad (37)$$

with  $F(x)$  an unknown function. This is the expected scaling form for  $S_{\text{topo}}(p, L)$ , assuming  $\gamma = 0$ , as well as  $S_a$ , when measured at  $t \propto L^z$ . To find the value of  $p_c$  and  $\nu$  that result in the best data collapse, we use the objective function  $\epsilon(p_c, \nu)$  which is defined as

$$\epsilon(p_c, \nu) = \sum_{i=2}^{n-1} (y_i - \bar{y}_i)^2, \quad (38)$$

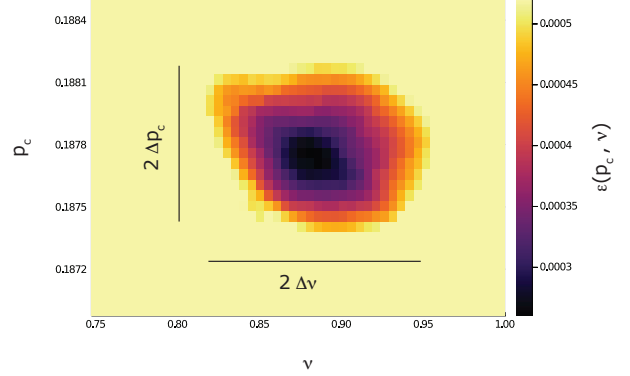


FIG. 7. The objective function as a function of  $p_c$  and  $\nu$  associated with the ancilla entropy data points near the percolation critical point shown in Fig.2b. Black denotes the minimum value  $\epsilon(p_c^*, \nu^*)$  and the light yellow correspond to values greater or equal to  $2\epsilon(p_c^*, \nu^*)$ . The corresponding error intervals are specified on the plot.

where

$$\bar{y}_i = y_{i-1} + \frac{y_{i+1} - y_{i-1}}{x_{i+1} - x_{i-1}}(x_i - x_{i-1}), \quad (39)$$

with  $y_i = S(p_i, L_i)$ ,  $x_i = (p_i - p_c)L_i^{1/\nu}$  and  $n$  is the total number of data points. The index  $i$  enumerates over all data points sorted such that  $x_1 < x_2 < \dots < x_n$ .  $\bar{y}_i$ , as defined in Eq.(39), is the expected value of  $y_i$  when it lies on the line passing through  $(x_{i-1}, y_{i-1})$  and  $(x_{i+1}, y_{i+1})$ . Hence, for a perfect collapse and in the limit of infinite data points, one gets  $\epsilon(p_c, \nu) = 0$ . Accordingly, to find the best collapse, we find  $p_c^*$  and  $\nu^*$  values which minimize the objective function  $\epsilon$ . To estimate the error in determining  $p_c^*$  and  $\nu^*$ , we find the interval around  $(p_c^*, \nu^*)$ , outside of which  $\epsilon(p_c, \nu) > 2\epsilon(p_c^*, \nu^*)$  (see Fig.7).

In case the scaling form has an extra scaling pre-factor, i.e.

$$S(p, L) = L^\gamma F((p - p_c)L^{1/\nu}), \quad (40)$$

we use basically the same procedure, but with  $y_i$  defined as  $y_i = S(p, L)/L^\gamma$  and using a slightly different objective function, defined as

$$\tilde{\epsilon}(p_c, \nu, \gamma) = \sum_{i=2}^{n-1} (\log(y_i) - \log(\bar{y}_i))^2. \quad (41)$$

We use  $\log(y_i)$  instead of  $y_i$  to make the objective function invariant under an overall rescaling of  $y_i$ . Otherwise, one can make the objective function in Eq.(38) arbitrarily small by choosing large enough  $\gamma$ .

Finally, the error bars for the best fit values of  $a$ ,  $b$  and  $\lambda$  parameters correspond to the standard errors found via least square fitting which reflects the quality of the fit.

## Supplementary Figures

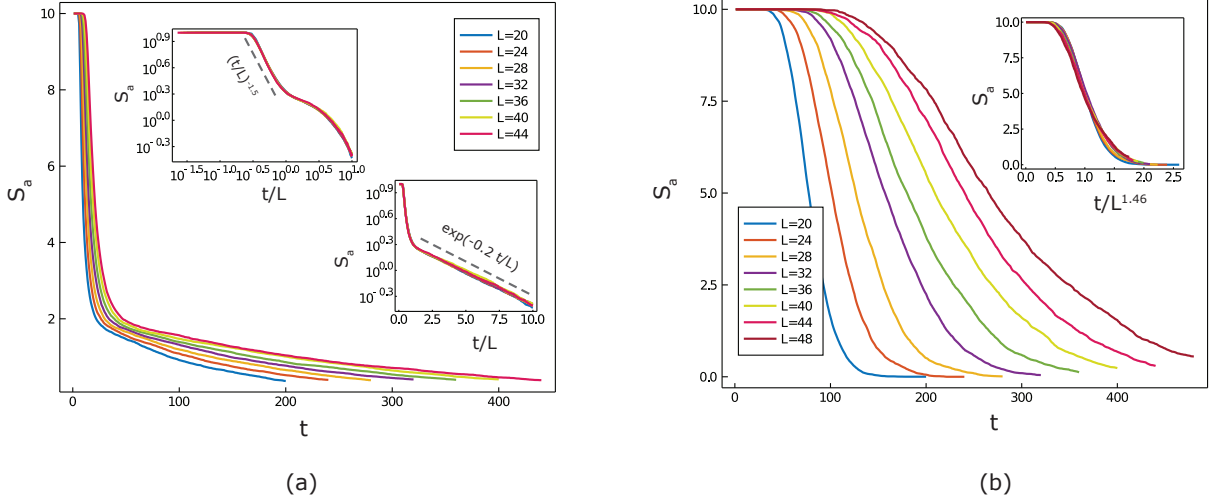


FIG. 8. (a) The ancilla entropy versus time at the percolation critical point, for different system sizes. The insets are the same quantity as a function of  $t/L$  in log-log and semi-log scales, showing that  $S_a$  is a function of  $(t/L)$  at the critical point in agreement with  $z = 1$ . Similar to  $(1+1)$ D circuits, the ancilla order parameter initially decays as a power law until  $t = O(L)$ , and then falls off exponentially. (b) the ancilla entropy versus time at the self-dual critical point  $(p_z, p_y) = (0, 0.5)$  which shows a quite different time-dependence at the self-dual critical point compared to the percolation critical point. By plotting  $S_a$  for different system sizes as a function of  $t/L^z$  for various  $z$ , we find  $z = 1.46$  results in the best collapse (shown in the inset), suggesting that the dynamical critical exponent at the self-dual critical point is  $z = 1.46(8)$ .

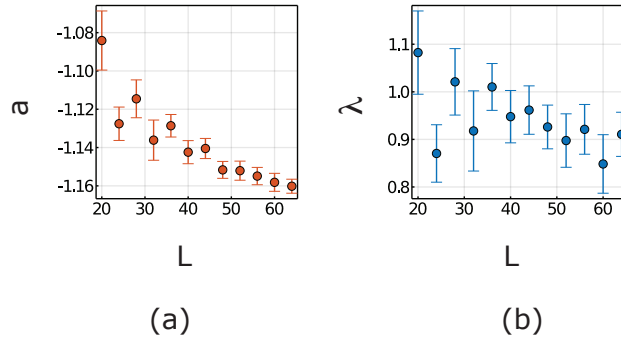


FIG. 9. The best fit value of the (a)  $a$  and (b)  $\lambda$  parameters of the  $S^{\text{qlm}}(x)$  scaling function at the percolation critical point (on the  $p_z$  axis for the projective and hybrid random circuits described in the main text (i.e.  $p_y = 0$  or  $p_u = 0$ , respectively). For the sub-leading term in  $S^{\text{qlm}}(x)$  to be universal,  $a$  and  $\lambda$  have to be independent of the system size. Although we observe a weak dependence of the  $a$  and  $\lambda$  on  $L$ , it could be either due to inherent error in pinpointing the exact location of the critical point or the finite size effects, in which case  $a$  and  $\lambda$  should plateau at large  $L$ s. Moreover note that  $\lambda$  parameter has rather large error bars, which is related to the nonlinear dependence of the  $S^{\text{qlm}}$  form on  $\lambda$ .

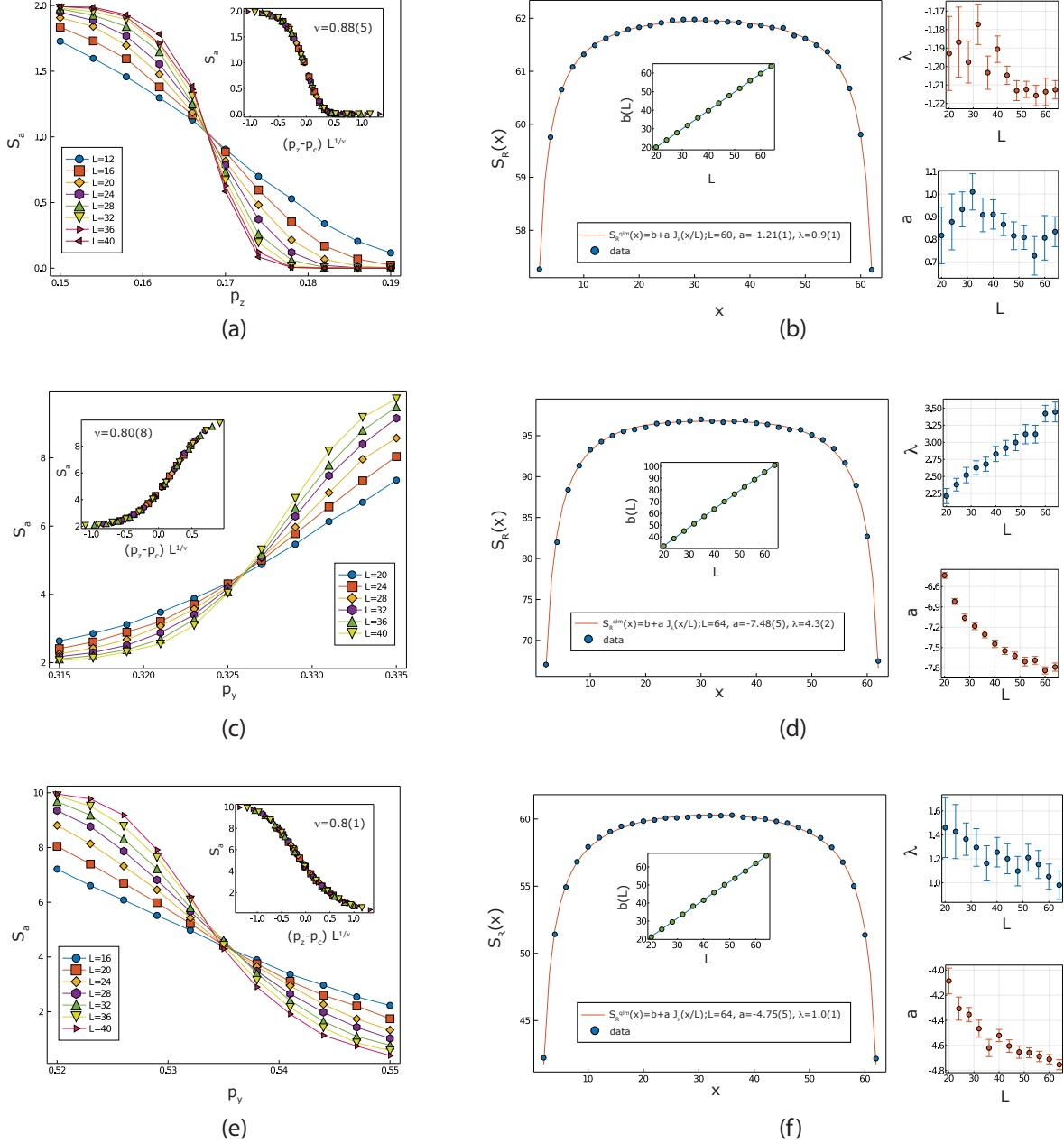


FIG. 10. Additional plots for the projective random circuit, showing a typical transition on the boundary of topological phase and trivial phase (first row), topological phase and volume law phase (second row) and volume law phase and trivial phase (third row). (a) the ancilla order parameter measured at  $t = 5L$  versus  $p_z$  for fixed  $p_y = 0.1$  near the topological to trivial phase transition with the corresponding collapse with  $p_c = 0.168(2)$  and  $\nu = 0.88(5)$  shown in the inset. (b) The entanglement of the cylindrical region,  $S_R(x)$ , as a function of  $x$  at  $(p_z, p_y) = (0.168, 0.1)$  for  $L = 64$ , with best fit of scaling function  $S_R^{\text{qlm}}$ . The inset shows the  $L$  dependence of the  $b$  parameter in  $S_R^{\text{qlm}}$  scaling function. On the right, is the  $L$  dependence of the best fit values of  $a$  and  $\lambda$  parameters versus  $L$ . (c)  $S_a$  measured at  $t = L$  versus  $p_y$  at fixed  $p_z = 0.1$  showing the phase transition from topological phase to volume law. The inset shows the corresponding data collapse with  $p_c = 0.326(1)$  and  $\nu = 0.80(8)$ . (d)  $S_R(x)$  as a function of  $x$  at  $(p_z, p_y) = (0.1, 0.326)$  with the best fit of  $S_R^{\text{qlm}}$  scaling function, with the inset, top right and bottom right panels showing the  $L$  dependences of best fit values of the parameters  $b$ ,  $\lambda$  and  $a$  respectively. (e)  $S_a$  measured at  $t = 3/2L$  versus  $p_y$  at fixed  $p_z = 0.1$  showing the phase transition from volume law phase to trivial. The inset shows the corresponding data collapse with  $p_c = 0.535(1)$  and  $\nu = 0.8(1)$ . (f)  $S_R$  at  $(p_z, p_y) = (0.1, 0.535)$  with best fit of scaling function  $S_R^{\text{qlm}}$ , the best fit value of  $b$  as a function of  $L$  (inset) and the best fit values of  $a$  and  $\lambda$  versus  $L$  on the right.

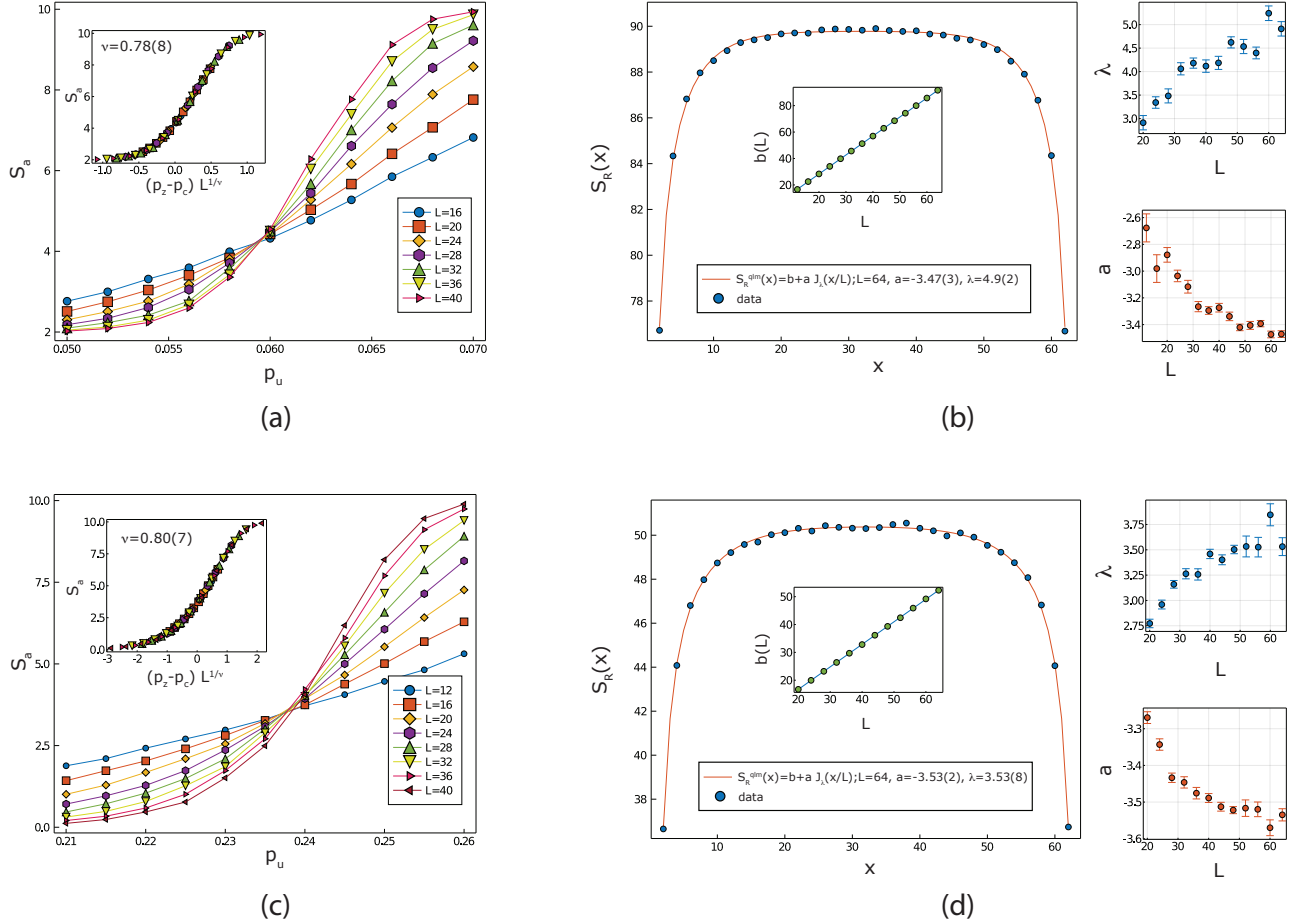


FIG. 11. Additional plots for the hybrid random circuit corresponding to the transitions from the topological phase to the volume law phase along the  $p_z = 0$  line (first row) and the phase transition from trivial phase to volume law phase along the hypotenuse  $p_z + p_u = 1$  (second row). (a) the ancilla order parameter measured at  $t = 3/4 L$  versus  $p_u$  along the  $p_z = 0$  axis near the topological to volume law phase transition with the corresponding collapse with  $p_c = 0.059(1)$  and  $\nu = 0.78(8)$  shown in the inset. (b) The entanglement of the cylindrical region,  $S_R(x)$ , as a function of  $x$  at  $(p_z, p_u) = (0, 0.059)$  for  $L = 64$ , with best fit of scaling function  $S^{\text{qlm}}$ . The inset shows the  $L$  dependence of the  $b$  parameter in  $S^{\text{qlm}}$  scaling function. The  $L$  dependence of the best fit values of  $a$  and  $\lambda$  parameters are shown on the right. (c)  $S_a$  measured at  $t = L$  versus  $p_u$  along the  $p_z + p_u = 1$  line, near the phase transition from trivial phase to volume law phase. The corresponding data collapse with  $p_c = 0.238(2)$  and  $\nu = 0.80(7)$  is shown in the inset. (d)  $S_R(x)$  as a function of  $x$  at  $(p_z, p_u) = (0.762, 0.238)$  with the best fit of  $S^{\text{qlm}}$  scaling function. The inset shows the  $L$  dependence of the  $b$  parameter in  $S^{\text{qlm}}$  scaling function, while the dependence of the best fit values of  $a$  and  $\lambda$  parameters is shown on the right.